JACS
JOURNAL OF THE AMERICAN CHEMICAL SOCIETY
pubs.acs.org/JACS
Article

Tuning the Intermolecular Electron Transfer of Low-Dimensional and Metal-Free BCN/C_{60} Electrocatalysts via Interfacial Defects for Efficient Hydrogen and Oxygen Electrochemistry

Md Ariful Ahsan, Tianwei He, Kamel Eid, Aboubakr M. Abdullah, Michael L. Curry, Aijun Du, Alain R. Puente Santiago,* Luis Echegoyen,* and Juan C. Noveron*

Cite This: *J. Am. Chem. Soc.* 2021, 143, 1203−1215

ABSTRACT: The development of low-dimensional (LD) supramolecular materials with multifunctional electrocatalytic properties has sparked the attention of the catalysis community. Herein, we report the synthesis of a new class of 0D−2D heterostructures composed of boron carbon nitride nanosheets (BCN NSs) and fullerene molecules (C_{60}/F) that exhibit multifunctional electrocatalytic properties for the hydrogen evolution/oxidation reactions (HER/HOR) and the oxygen evolution/reduction reactions (OER/ORR). The electrocatalytic properties were studied with varying F:BCN weight ratios to optimize the intermolecular electron transfer (ET) from the BCN NSs to the electron-accepting C_{60} molecules. The nanohybrid supramolecular material with 10 wt % F in BCN NSs (10% F/BCN) exhibited the largest Raman and C 1s binding energy shifts, which were associated with greater cooperativity interactions and enhanced ET processes at the F/BCN interface. This synergistic interfacial phenomenon resulted in highly active catalytic sites that markedly boosted electrocatalytic activity of the material. The 10% F/BCN showed the highest tetrafunctional catalytic performance, outperforming the OER catalytic activity of commercial RuO_2 catalysts with a η_{10} of 390 mV and very competitive onset potential values of −0.042 and 0.92 V vs RHE for HER and ORR, respectively, and a current density value of 1.47 mA cm^{-2} at 0.1 V vs RHE with an ultralow ΔG_{H^*} value of −0.03 eV toward the HOR process. Additionally, the 10% F/BCN catalyst was also used as both cathode and anode in a water splitting device, delivering a cell potential of 1.61 V to reach a current density of 10 mA cm^{-2}.

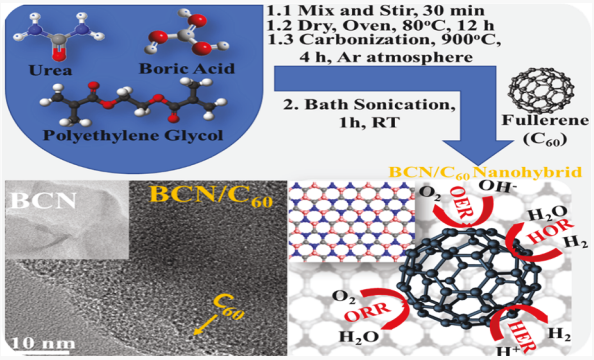

1. INTRODUCTION

Low-dimensional catalytic materials have recently impacted the scientific community as promising functional building blocks to construct highly efficient supramolecular nanoscale structures for water electrocatalysis.[1,2] A wide portfolio of heterostructures can be obtained from the noncovalent integration of 0D, 1D, and 2D nanomaterials into 0D−1D, 0D−2D, 1D−2D, and 2D−2D hybrids to achieve sustainable alternatives for advanced electrocatalytic systems.[3] The electronic structures and catalytic performances of supramolecular nanoassemblies have been starting to be tailored by controlling the interfacial interactions between their components, thus paving the way toward a new generation of tunable molecular electrocatalysts.[4,5] Among them, the noncovalent heterostructures based on metal-free carbon nanomaterials are gaining special interest due to their unique physicochemical properties such as large surface areas, excellent electronic and mechanical properties, and their affordable prices,[6] which allow them to compete with the traditional noble-metal-based electrocatalysts. In addition, noble-metal-based electrocatalysts often undergo several problems associated with their high prices, susceptibility to CO poisoning, low durability, and selectivity, which obstruct their applications for fuel cell technologies.[6] Therefore, it is of utmost interest to develop highly stable and durable metal-free carbon-based electrocatalysts with higher electrochemical activities for a sustainable future.

Remarkably, some new non-metal-based catalysts have exhibited excellent activities for oxygen and/or hydrogen electrochemistry under a broad range of pH, outperforming by far the catalytic activity and the long-term electrochemical stability properties of conventional benchmark catalysts, including Pt and RuO_2.[4] For instance, experimental and theoretical studies have confirmed that the high catalytic

Received: November 27, 2020
Published: January 5, 2021

https://dx.doi.org/10.1021/jacs.0c12386
J. Am. Chem. Soc. 2021, 143, 1203−1215

activities of low-dimensional heterostructures such as 0D−1D graphene quantum dots/graphene nanoribbons[7] and 1D−2D CNT/graphene[8] are ascribed to the efficient intramolecular charge transfer processes between their intimately contacted components, which result in abundant and highly accessible catalytic active sites. Among the most promising metal-free 2D platforms to fabricate supramolecular hybrid electrocatalytic nanomaterials, boron carbon nitride nanosheets (BCN NSs) have the desirable physicochemical properties of both 2D hexagonal boron nitride (h-BN) and graphene.[9−12] They can also act as high-performance nanoplatforms for energy-related purposes due to their unique electrical conductivity, mechanical and chemical stability, and the synergistic N and B heteropolar bonding contribution, which can increase the electroactivity rates.[13−17] Up to now, BCN nanostructures have achieved notable results in oxygen reduction (ORR) and hydrogen evolution (HER) reactions, delivering excellent yields in both alkaline and acid solutions.[18,19]

Despite these remarkable results, the electrocatalytic performance of BCN nanosheets and other emerging nonmetal 2D nanomaterials have not been improved yet because their electronic, physical, and chemical properties are confined in a 2D structure, and the number of catalytic centers as well as their intrinsic performances cannot be easily tailored, thus limiting their further applications for electrocatalysis.[2] Therefore, the interface engineering of 2D nanostructures with other LD architectures could expand their potential to develop new nano-electrocatalytic systems. In this sense, the short-range interfacial interactions of two LD materials can promote plenty of high-speed electron pathways and a simultaneous electronic coupling, thus speeding up the ET processes at the interface as well as optimizing the energy adsorption states of the intermediate catalytic species.[1,6] Buckminsterfullerene (C_{60}) is a 0D carbon structure that exhibits extraordinary electron-accepting properties and high affinity to construct supramolecular assemblies, thus becoming strong candidates to build efficient multifunctional metal-free hybrid electrocatalysts.[1,20−22] The integration of C_{60} molecules into the BCN network could generate new tunable interfacial active sites as a consequence of the electronic flow between both LD materials, thus boosting the electrocatalytic properties of the assembled materials compared with their individual components.

To the best of our knowledge, no report of supramolecular boron carbon nitride and fullerene-based nano-heterostructures for high-performance electrocatalysis has been published. In this work, we fabricated a novel class of supramolecular metal-free and low-dimensional 0D−2D nanohybrids using zero-dimensional C_{60} molecules and two-dimensional BCN nanosheets. The 0D−2D nanohybrids were constructed by varying the F/BCN weight ratios (5% F/BCN, 10% F/BCN, 20% F/BCN, and 30% F/BCN) to form nonmetallic multifunctional electrocatalysts for HER, HOR, OER, and ORR reactions that exhibit better electrocatalytic properties compared to their individual components. The multifunctional electrocatalytic activity of F/BCN nanoassemblies was finely tuned with the local structural defects at the 0D−2D interfaces. The fullerene/BCN interfacial interactions induced slight distortions on the planar sp^2 BCN surfaces, allowing the electronic coupling between the BCN NSs and fullerenes and the formation of interfacial catalytic sites. Importantly, XPS and Raman experiments also demonstrated that the effectiveness of the electronic coupling depends on the weight percentages of the fullerene molecules, which markedly influence the intrinsic catalytic activity of the interfacial catalytic sites and, in turn, the overall multifunctional electrocatalytic performances of the 0D−2D catalysts. This report provides a deep insight into the structure/catalytic function of C_{60}-BCN via a thorough combination of theory and experiment.

2. EXPERIMENTAL SECTION

2.1. Materials. All reagents were purchased and used as received without any further purification. Poly(ethylene glycol) (PEG), boric acid (H_3BO_3), urea, fullerene (C_{60}/F), ethanol, isopropyl alcohol (IPA), sodium hydroxide, sulfuric acid, phosphate-buffered saline (PBS), Nafion solution (5 wt %), Pt/C (20%), and ruthenium oxide (RuO_2) were purchased from Sigma-Aldrich. Deionized water (DW, 18 MΩ/cm) was obtained from the Milli-Q instrument.

2.2. Synthesis of F/BCN Electrocatalysts. Initially, the boron carbon nitride nanosheet precursors were prepared to obtain the desired F/BCN electrocatalysts. Urea (10 g), boric acid (0.3 g), and PEG-2000 (2 g) were first dissolved in 60 mL of water in a 100 mL beaker under continuous stirring until a transparent solution was observed. The solution was then dried in an oven at 80 °C for 12 h. Subsequently, the obtained solid was carbonized at 900 °C with a 5 °C/min for 4 h under an argon atmosphere. The black powder (BCN NSs) was collected after the tubular furnace cooled to room temperature. For making the F/BCN electrocatalysts, 50 mg of BCN NSs powder was placed in a beaker, mixed with 20 mL of IPA, and sonicated for 30 min. Considering that the IPA is soluble in toluene, a fullerene solution in toluene (from 5 to 30 wt %) was then added slowly to the BCN NSs solution and then bath sonicated for 30 min to form the F/BCN nanohybrids. The nanohybrids were then collected by centrifugation followed by washing with toluene and water several times and then dried at 70 °C for overnight in a vacuum oven.

2.3. Materials Characterization. X-ray diffraction (XRD) patterns of the electrocatalysts were recorded on a Bruker D8 Discover X-ray diffractometer. The morphological analysis of the nanohybrids was performed on a transmission electron microscope (Tecnai G220, FEI, Hillsboro, OR) and on a high-angle annular dark-field scanning transmission electron microscope (HAADF-STEM) at 200 kV, and elemental analyses were conducted by using an energy-dispersive spectrometer (EDS) which was equipped with the STEM instrument. The surface chemical analysis of the nanohybrids was done by X-ray photoelectron spectroscopy on a Kratos Axis spectrometer (Ultra DLD XPS Kratos, Manchester, UK). The Raman spectroscopic study of the nanohybrids was recorded by using a DXR Smart Raman instrument (Thermo Scientific) under diode laser excitation of ∼532 nm.

2.4. Electrochemical Measurements. The electrochemical measurements were done by using a three-electrode system on an electrochemical workstation. A glassy carbon, a graphite rod, and Ag/AgCl were used as the working, counter, and reference electrodes, respectively. To prepare the catalyst ink for the working electrode, 1 mg of the F/BCN nanohybrids and 30 μL of Nafion solution (5 wt %) were dispersed in 1 mL of ethanol. The slurry was then bath sonicated for 30 min to form a homogeneous ink. Afterward, 10 μL of the catalyst ink was deposited on the working electrode and dried in air. All electrodes were made by depositing the same amount of catalyst ink on the working electrode by using the same methodology. Linear sweep voltammetry (LSV) measurements were performed at a scan rate of 2 mV s^{-1} in an electrolyte solution (0.5 M H_2SO_4 for HER and HOR processes, 0.5 M NaOH for OER and ORR processes). The mass activity (MA), specific activity (SA), and turnover frequency (TOF) values were calculated at −0.4, 1.7, and 0.65 V for the HER, OER, and ORR processes, respectively. The overall water splitting experiments including the fabrication of carbon cloth electrodes were conducted following a previously reported method.[23] All the voltage values were referenced to the reversible hydrogen electrode (RHE) by using the following equation:[24]

https://dx.doi.org/10.1021/jacs.0c12386
J. Am. Chem. Soc. 2021, 143, 1203−1215

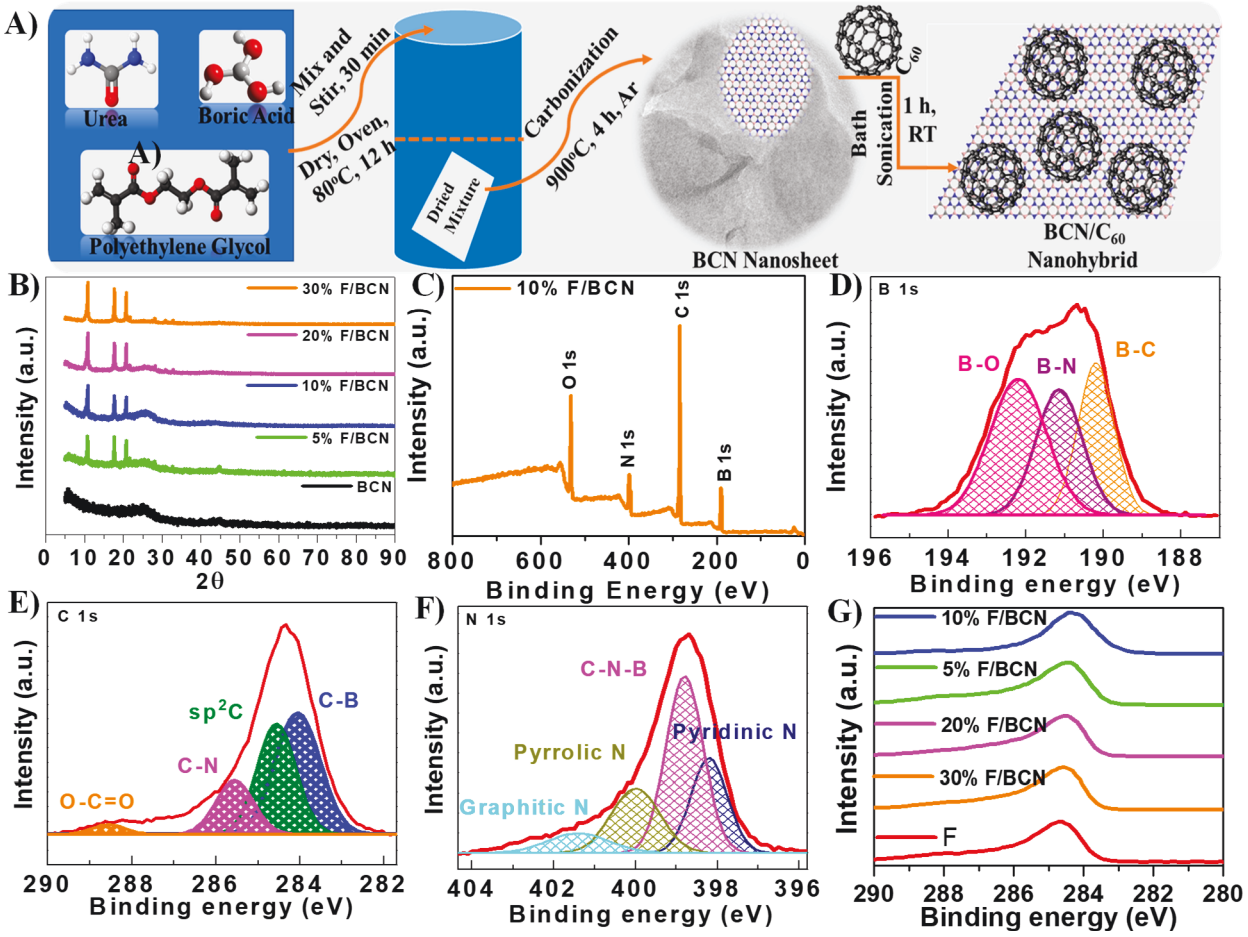

Figure 1. (A) Schematic representation of the synthesis of F/BCN nanohybrids. (B) XRD analysis of the nanohybrids. (C–F) XPS survey spectra, high-resolution XPS B 1s, C 1s, and N 1s spectra of 10% F/BCN nanohybrid, respectively. (G) Comparison of C 1s spectra for F, 5% F/BCN, 10% F/BCN, 20% F/BCN, and 30% F/BCN nanohybrids.

$$E_{RHE} = E_{Ag/AgCl} + 0.197\ V + 0.059pH \quad (1)$$

Afterward, the following Tafel equation was used to calculate the Tafel slope to investigate the electrocatalytic performances as well as the kinetics of the HER/OER/ORR processes[24]

$$\eta = a + b \log j \quad (2)$$

where j, η, a, and b are the current density, overpotential, transfer coefficient, and Tafel slope, respectively.

A glassy carbon disc (5 mm in diameter, Pine Instruments Company) was used as the working electrode in the rotating disc electrode (RDE) experiments. All electrochemical measurements were conducted within a potential range from 0.1 to −0.60 V vs Ag/AgCl at a scan rate of 10 mV s^{-1}. All potentials were referenced to the RHE. The kinetic parameters were assessed by using the following Koutecky–Levich (K–L) equations[24,25]

$$\frac{1}{J} = \frac{1}{J_L} + \frac{1}{J_K} = \frac{1}{B\omega^{1/2}} + \frac{1}{J_K} \quad (3)$$

$$B = 0.20nFC_O D_O^{2/3} \nu^{-1/6} \quad (4)$$

where J, J_K, and J_L are the measured, kinetic-limiting, and diffusion-limiting current densities, respectively; n is the transferred number of electrons for the ORR process, ω is the angular velocity, F is the Faraday constant, C_O is the bulk concentration of oxygen (1.2×10^{-6} mol cm^{-3}), ν is the kinematic viscosity of the electrolyte (0.01 cm^2 s^{-1}), and D_o represents the oxygen diffusion coefficient which exhibits a value of 1.9×10^{-5} cm^2 s^{-1}.

3. RESULTS AND DISCUSSION

3.1. Structural Characterization. In a typical synthetic process, a F/toluene solution was gently injected into a BCN NSs/IPA solution under constant bath sonication. This formed a dark brown interface in between the two liquid phases, indicating the formation of the F/BCN nanohybrids. The diffusion of both components from their respective solutions led to the formation of the interface. The attachment of fullerene molecules onto the BCN NSs surfaces occurs via a $\pi-\pi$ stacking interaction. Finally, the fullerene-decorated BCN NSs can be obtained by centrifugation of the solution. The schematic diagram for the synthesis of F/BCN nanohybrids is presented in Figure 1A.

The BCN NSs and F/BCN nanohybrid samples were characterized by X-ray powder diffraction (XRD), and the results are presented in Figure 1B. The XRD pattern of BCN NSs displayed two characteristic bands at around 25° and 44°, which typically represent the 002 and 101 interlayer reflections of the BCN, respectively.[26] On the other hand, the XRD pattern of F/BCN nanohybrids showed several diffraction peaks at around 10.83°, 17.72°, 20.76°, 21.70°, 27.56°, 28.23°, 30.94°, and 32.86°, which correspond to the (111), (220), (311), (222), (331), (420), (422), and (511) diffraction planes of F, respectively, in addition to showing the diffraction pattern of BCN as well.[4,27] Upon the interaction of F with BCN NSs, the BCN diffraction peak (002) is slightly shifted to

https://dx.doi.org/10.1021/jacs.0c12386
J. Am. Chem. Soc. 2021, 143, 1203−1215

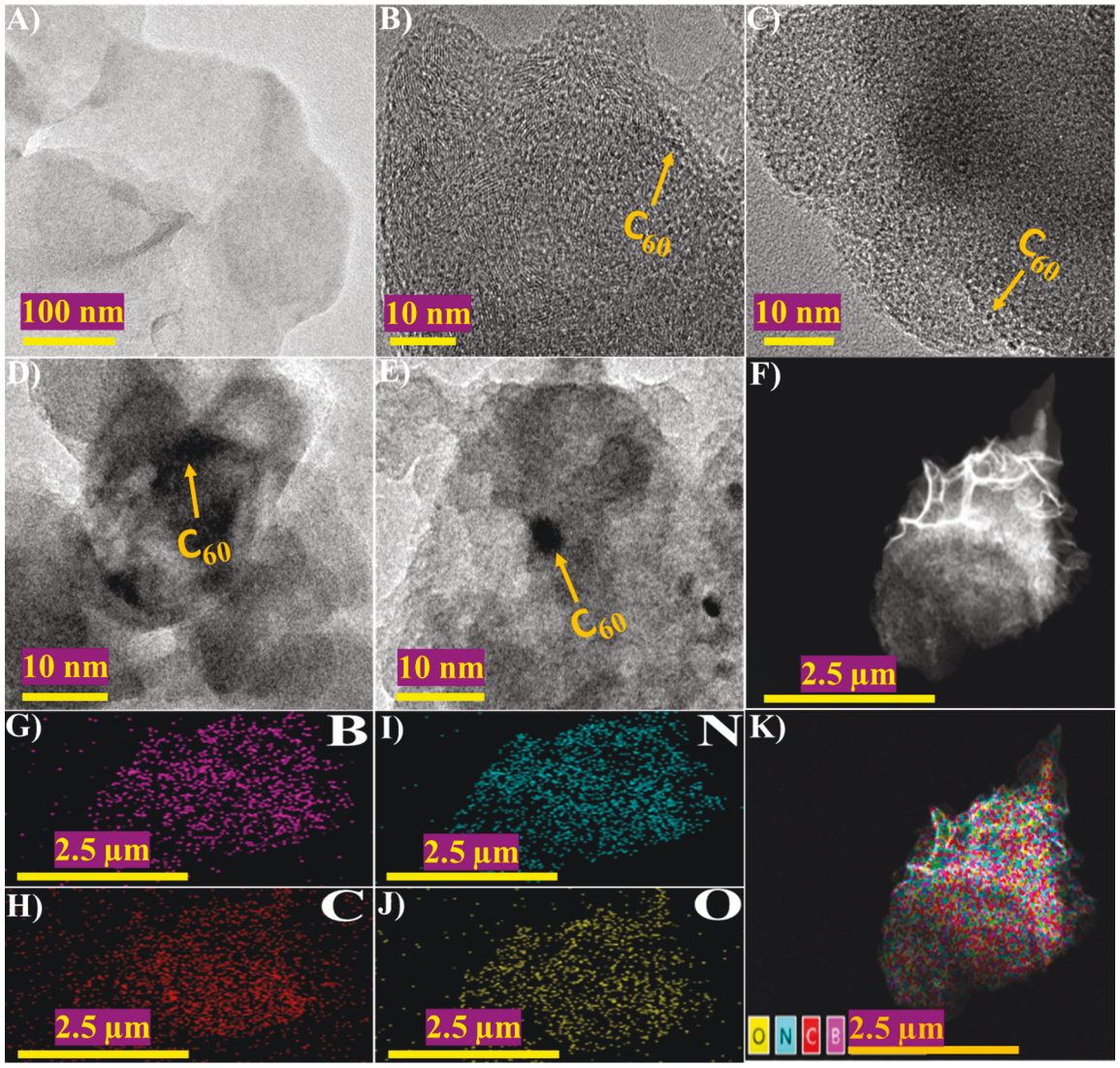

Figure 2. (A–E) STEM images of BCN NSs, 5% F/BCN, 10% F/BCN, 20% F/BCN, and 30% F/BCN nanohybrids, respectively. (F–K) High-angle annular dark field (HAADF) STEM image and elemental mapping of 10% F/BCN, showing the presence of B, C, N, and O.

~25.5°. The XRD spectra of all F/BCN nanohybrids in Figure 1B show a higher degree of crystallization, suggesting a good charge mobility as well as electrochemical stability. The XRD patterns demonstrated that the fullerenes had been successfully incorporated onto the BCN NSs surface.

Raman spectroscopy is a nondestructive and fast technique that can provide insightful information about the lattice and electronic structures of carbon-based nanomaterials.[4] Raman spectra of the BCN NSs, pristine F, and F/BCN nanohybrids are presented in Figure S4. The BCN NSs display two sharp peaks at around 1345 and 1588 cm^{-1} for the D- and G-bands, respectively.[19] Generally, the D-band reflects the defects or lattice distortion of the carbons, while the G-band represents the graphitic and crystallization degree of the carbon-based materials.[4,19] The Raman spectra of F shows a sharp peak at around 1466 cm^{-1}, which is characteristic for the fullerene molecule due to the pentagonal pinch mode $A_g(2)$.[5,28] On the other hand, the F/BCN nanohybrids showed the presence of all three Raman bands (D- and G-band for BCN NSs and pentagonal pinch $A_g(2)$ mode for fullerene) with a slight shift, indicating the successful synthesis of F/BCN hybrids. For instance, the G-band for BCN NSs shifts from 1588 to 1598 cm^{-1} for the 10% F/BCN hybrid, demonstrating a charge transfer from the BCN NSs to the fullerene.[4,28,29] The intensity ratio of the D- to G-band (I_D/I_G) was also calculated and found to be 0.971, 1.014, 1.046, 0.996, and 0.994 for the BCN, 5% F/BCN, 10% F/BCN, 20% F/BCN, and 30% F/BCN, respectively. While the upshift of the peak positions supports the charge transfer process from BCN NSs to the electron-accepting F, the increase in the I_D/I_G values for F/BCN nanohybrids demonstrates that the nanosheet structure became a little more disordered.[4] Interestingly, the 10% F/BCN nanohybrid displayed the highest I_D/I_G value among all the nanohybrids, indicating the presence of more structural defects, and the shift in the G-band is also higher, suggesting that the charge transfer process is more favored, which could lead to better electrocatalytic performance.[4,24] On the basis of the findings from the Raman analysis, it was confirmed that F was successfully attached to the BCN NSs, and charge transfer occurred between the BCN NSs and the fullerene molecules.

X-ray photoelectron spectroscopic (XPS) measurements were conducted to verify the intermolecular charge transfer process between the BCN NSs and fullerene molecules that was observed by the Raman analysis as well as to elucidate the

https://dx.doi.org/10.1021/jacs.0c12386
J. Am. Chem. Soc. 2021, 143, 1203–1215

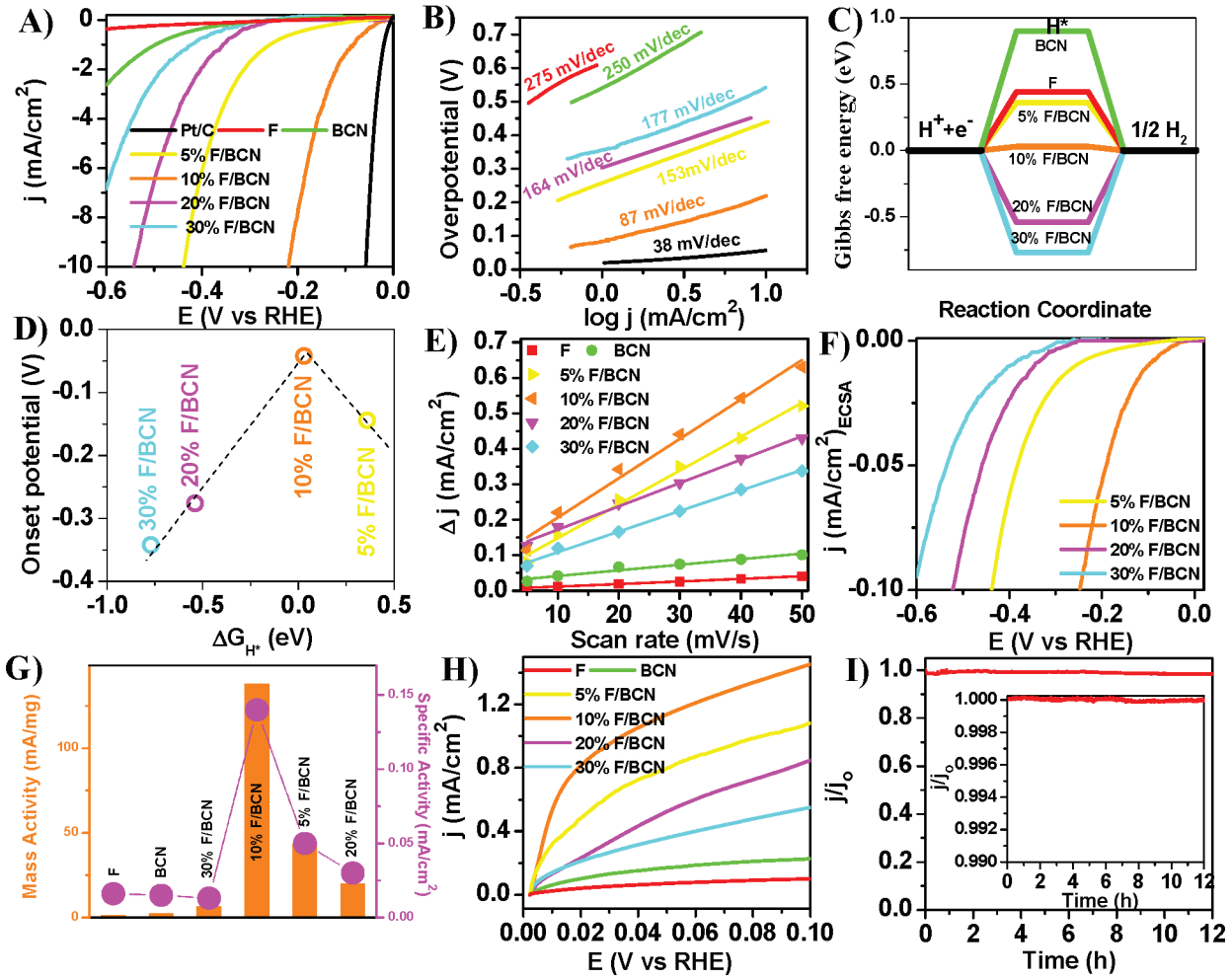

Figure 3. (A) Representative HER LSVs for F, BCN, 5% F/BCN, 10% F/BCN, 20% F/BCN, 30% F/BCN, and commercial Pt/C at 2 mV s^{-1} in 0.5 M H_2SO_4. (B) The corresponding Tafel plots. (C) Free energy changes (ΔG_{H^*}) of H adsorption on F, BCN, and their nanohybrids. (D) Volcano plots of onset potential vs ΔG_{H^*} for the hybrid catalysts. (E) Differences of anodic and cathodic current densities vs scan rates of the catalysts at 0.2 V vs RHE. (F) ECSA normalized HER LSV curves for F/BCN nanohybrids. (G) MA and SA trends for F, BCN, and their hybrids. (H) Steady-state polarization curves for F, BCN, and their nanohybrids for HOR in H_2-saturated 0.5 M H_2SO_4. (I) Chronoamperometric plots of 10% F/BCN for HER and HOR (inset) at −0.35 and 0.09 V vs RHE, respectively.

chemical compositions. The results are presented in Figure 1C−F. As expected, it was found that the 10% F/BCN nanohybrid contained B, C, N, and O elements with sharp XPS bands (Figure 1C). The XPS analysis also clearly confirmed the absence of any metal content in the 10% F/BCN sample, demonstrating the metal-free nature of the sample. To further elucidate the chemical nature of the 10% F/BCN nanohybrid, the high-resolution XPS spectra of B, C, and N were inspected. As seen in Figure 1D, the high-resolution B 1s spectra could be deconvoluted into three different peaks for B−N, B−C, and B−O bonds.[19,30] Furthermore, the deconvolution of the C 1s band shows four types of peaks indicating the presence of B−C, C−N, sp^2 (C═C), and O−C═O (Figure 1E).[19,30−32] The higher content of sp^2 (C═C) suggests that the C═C bonds dominate for the BCN NSs conjugated framework. Moreover, the high-resolution N 1s spectra were deconvoluted into four peaks that correspond to the graphitic N, pyrrolic N, pyridinic N, and C−N−B (Figure 1F).[31,33] Remarkably, there is a very significant content of pyridinic N and C−N−B, inferring that a higher number of ORR electroactive sites exist in the 10% F/BCN nanohybrid.[19] The peak position of C 1s XPS spectra for F/BCN hybrids showed a negative shift to the lower binding energies (BE) as compared to the C 1s spectra of pure fullerene, indicating the existence of intermolecular charge transfer processes from the BCN NSs to F (Figure 1G).[4] The shift of the XPS band toward the lower BE values demonstrates the progressive distortion of the sp^2 BCN planar structure, which increases the electronic coupling between F and BCN NSs at the same time. Notably, the negative shift of the C 1s spectra (284.63 to 284.33 eV) for the 10% F/BCN hybrid is higher than for the other samples, indicating that the intermolecular charge transfer process is more pronounced for the 10% F/BCN hybrid, which can improve its electrocatalytic activity.[4] This observed intermolecular charge transfer trend is also in good agreement with the findings from the Raman analysis.

The UV−vis spectra of F and 10% F/BCN were also obtained, and the results are presented in Figure S5. The UV−vis spectrum of F displayed a characteristic band at around 328 nm, which is usually results from the $\pi-\pi$ electronic transitions.[34] The red-shift in the band located at around 328 nm is associated with the interactions between F and the other molecules, and therefore this band is a key indicator for the interactions of F with aromatic rings.[35] The $\pi-\pi$ stacking

https://dx.doi.org/10.1021/jacs.0c12386
J. Am. Chem. Soc. 2021, 143, 1203−1215

of F and BCN NSs likely delocalizes the π-electron system and thereby reduces the required energy for the electronic transitions. The band at 328 nm for F shifts to 335 nm for 10% F/BCN, demonstrating that the F is successfully attached to the BCN nanosheets, and the $\pi-\pi$ interactions significantly facilitate the formation of F/BCN nanohybrids. Scanning transmission electron microscopic (STEM) analyses were conducted to further investigate the microstructure of the BCN NSs and F/BCN nanohybrids, and the images are presented in Figure 2A−E. BCN NSs display a smooth and sheetlike structure without particles on their surfaces (Figure 2A).[19] By contrast, the morphological analysis of the 5% F/BCN and 10% F/BCN nanohybrids in Figure 2B,C reveals that some fullerene molecules are uniformly dispersed on the surface of BCN NSs. As indicated by the yellow arrows in Figure 2B,C, the F molecules with sizes ∼0.9 nm are distributed on the BCN nanosheet layers. There were no apparent differences in the F size when the F concentration was increased from 5 to 10%, which could be due to the fact that changing of F concentration from 5% to 10% might not facilitate fullerene aggregation.[36] Furthermore, the F-decorated BCN nanosheets prepared at higher F concentrations (20% and 30%) showed big clusters of fullerene molecules on the BCN nanosheet surfaces (indicated by the yellow arrow) with broader size distributions compared to the ones prepared at lower concentrations (5% and 10%), as seen in Figure 2D,E. The increase in the agglomerated fullerene domains for the 20% F/BCN and 30% F/BCN composites should have resulted from the higher F concentration, which tends to create larger seeds for the nanoparticle growth.[36,37] On the other hand, the F/BCN composites with lower F concentrations (5% and 10%) displayed single- or few-layered structures that likely result from the attached fullerene molecules, which serve as spacers and can effectively prevent the BCN nanosheets from restacking and agglomeration during the processing in solution. However, agglomerated or multilayered structured BCN NSs were observed in the case of higher F-containing nanohybrids (20% and 30%), where the clusters of F molecules formed on the BCN surfaces cannot effectively prevent the BCN NSs from restacking or agglomeration as seen in Figure 2D,E and thus can impact the electrocatalytic performances negatively. The STEM-EDS elemental mapping verified the presence of all of the expected elements (B, C, N, and O) and also showed that all the elements are distributed evenly on the nanosheets, as seen in Figure 2F−K.

3.2. Hydrogen Evolution and Oxidation Reactions. We explored the catalytic function of the F/BCN nanohybrids for hydrogen evolution and oxidation reactions using a combination of experimental and theoretical techniques to obtain a comprehensive understanding of the correlation between the structural properties of the hybrids, particularly the interfacial 0D−2D interactions and their electrocatalytic performances. The LSV polarization curves of the HER process in 0.5 M H_2SO_4 solution were recorded for F, BCN, 5% F/BCN, 10% F/BCN, 20% F/BCN, and 30% F/BCN as well as for the Pt/C benchmark, and the results are shown in Figure 3A. Notably, the incorporation of the fullerene molecules on the top of BCN NSs resulted in the formation of very active electrocatalysts with higher electrocatalytic rates that exceed the catalytic activity of their individual components, thus suggesting that the interfacial interactions enhance the HER electrocatalytic activity of the low-dimensional nanohybrids. While the onset potential for F and BCN NSs were estimated to be −0.529 and −0.394 V vs RHE, respectively, the nanohybrid structures achieved enhanced HER onset potentials of −0.144, −0.042, −0.276, and −0.342 V vs RHE for 5% F/BCN, 10% F/BCN, 20% F/BCN, and 30% F/BCN, respectively. To investigate the kinetics of the HER process, we calculated the Tafel slopes for each catalyst using the Tafel equation (eq 2) from the respective LSV polarization curves in Figure 3A. The Tafel slopes showed the same electrocatalytic trend (Figure 3B). The hybrids resulted in lower Tafel slopes (153, 87, 164, and 177 mV/dec for 5% F/BCN, 10% F/BCN, 20% F/BCN, and 30% F/BCN, respectively) compared with those for F (275 mv/dec) and BCN NSs (250 mV/dec), indicating that the fullerene/BCN interfaces improve the electrokinetics of the HER process as well. Lower Tafel slopes indicate better HER kinetics; thus, the 10% F/BCN nanohybrid displayed the best HER kinetics among the systems studied (Figure 3B). The mechanism of the F/BCN nanohybrid mediated HER processes in acidic media can be described by three possible steps. The first step is known as the Volmer step, in which a hydrogen atom is adsorbed on the catalyst surface.[24]

$$H_3O^+ + e^- + F/BCN \rightarrow F/BCN{-}H_{ads} + H_2O \quad (5)$$

The Volmer step is followed either by the Heyrovsky step (electrochemical desorption)

$$F/BCN{-}H_{ads} + e^- + H^+ \rightarrow F/BCN + H_2 \quad (6)$$

or the Tafel step (chemical desorption)

$$2F/BCN{-}H_{ads} \rightarrow 2F/BCN + H_2 \quad (7)$$

The theoretical Tafel slopes of Tafel, Heyrovsky, and Volmer reactions are 30, 40, and 120 mV/dec, respectively.[25] The obtained Tafel slope for 10% F/BCN suggests that the 10% F/BCN-mediated HER reaction follows a Volmer−Heyrovsky mechanism, with the Heyrovsky step being the rate-determining one.

The superior catalytic performances of the hybrid supramolecular architectures can be ascribed to the interfacial synergism between the components that promote the intermolecular electron transfer (ET) from the 2D BCN nanosheets to the electron-accepting fullerenes, thus leading to a net negative charge density on the fullerene cages and thereby favoring the proton adsorption step and the overall HER activity.[4] The lone pair electrons on the N atoms interact with the vacant $2p_z$ orbitals of the B atoms on the BCN framework, which inhibits electronic conjugation with the π-systems.[38] But the distortion of the planar sp^2 BCN network induced by the fullerene interactions slightly elongates the B−N distances, which enhance the electronic coupling of the N lone pair electrons with the π clouds delocalized around the fullerene structure,[38] thus allowing an effective electronic coupling between the BCN and fullerene molecule. As a result, the electrons gathering at the fullerene surfaces create very active interfacial catalytic sites that can optimize the energy adsorption states of the intermediate catalytic species, thus enhancing the electrocatalytic HER activity. As stated in the characterization section using the I_D/I_G ratios, the number of structural defects follows the trend 10% F/BCN > 5% F/BCN > 20% F/BCN > 30% F/BCN, which matches perfectly with both the XPS shifts to lower binding energies and the electrocatalytic rates, indicating that the interfacial defects on

https://dx.doi.org/10.1021/jacs.0c12386
J. Am. Chem. Soc. 2021, 143, 1203−1215

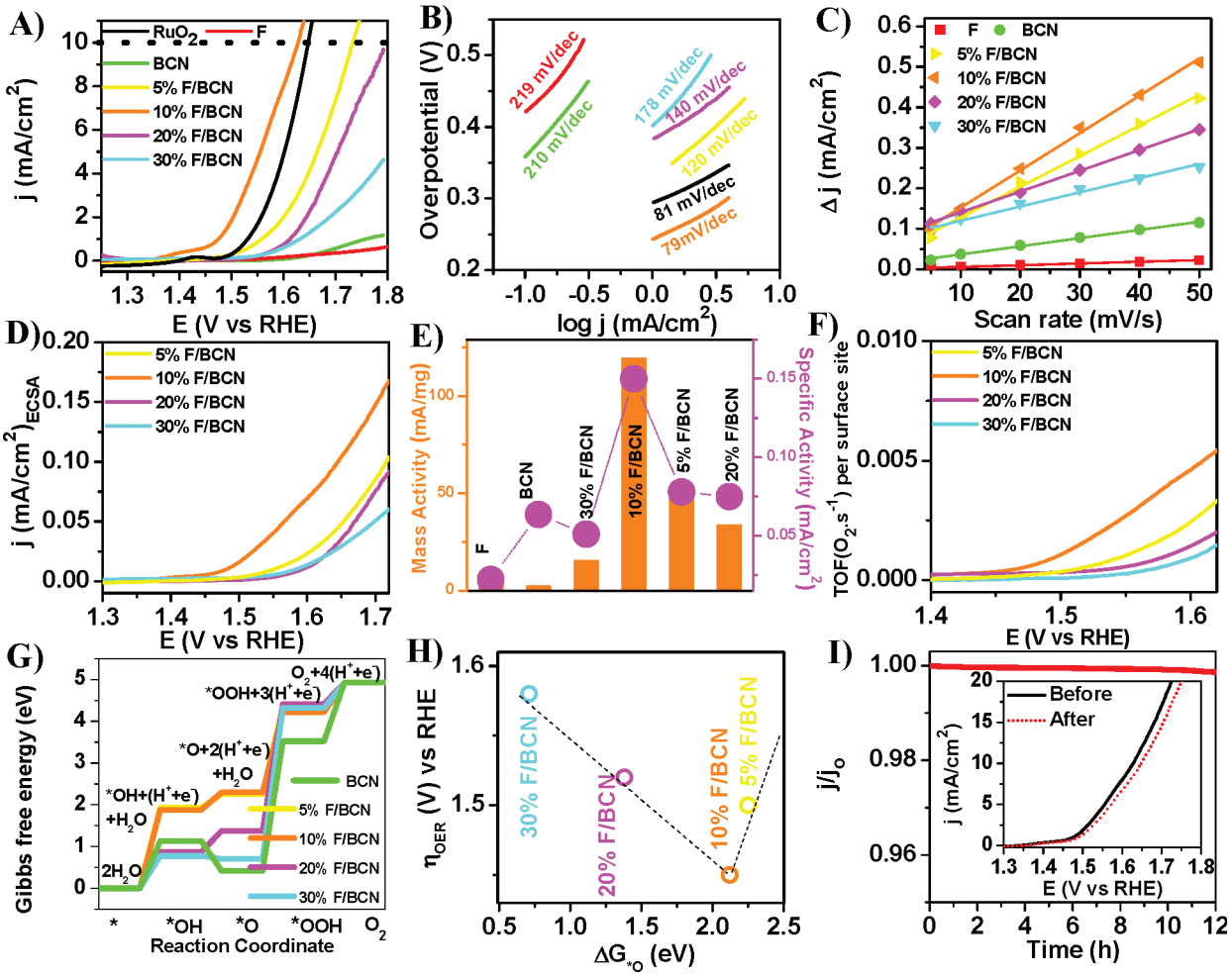

Figure 4. (A) OER LSV polarization curves for F, BCN, 5% F/BCN, 10% F/BCN, 20% F/BCN, 30% F/BCN, and RuO_2 benchmark catalyst at 2 mV s^{-1} in 0.5 M NaOH. (B) Their respective Tafel plots. (C) Differences of anodic and cathodic current densities vs scan rates at 1.2 V vs RHE. (D) LSV polarization curves normalized by ECSA for the F/BCN catalysts. (E) Comparison of intrinsic OER catalytic activities in terms of MA and SA. (F) OER LSVs normalized by the TOF for all F/BCN nanohybrids. (G) changes in Gibbs free energy of each elementary reaction step toward OER for both BCN and LD hybrids. (H) The volcano plots of η_{OER} vs ΔG_{*O}. (I) chronoamperometric measurement of 10% F/BCN at 1.70 vs RHE and the comparison of LSV curve before and after 1000 CV cycles (inset).

the catalysts regulate the efficiency of the ET process as well as the HER catalytic rates. Furthermore, the 5% F/BCN and 10% F/BCN catalysts, which are by far the best catalytic nanomaterials, show a very well-dispersed fullerene distribution pattern on the BCN surfaces (see STEM pictures). The uniform fullerene distribution hinders the restacking of the BCN NSs, providing more exposed active sites as well as higher electronic conductivity throughout the nanosheet network. It can favor both the distortion of the heteroatom groups of the sp^2 carbon framework and the intermolecular charge-transfer rates, giving rise to ultraactive catalytic spots at the F/BCN electrochemical interfaces. In contrast, the aggregation of fullerenes for the 20% and 30% F/BCN hybrid samples allows the restacking of the BCN NSs, thus reducing the number of exposed active sites, surface defects, and ET processes, thereby resulting in a lower catalytic activity for the HER process. Besides, the accessibility of the protons to the active sites of the aggregated fullerene/BCN interfaces would be strongly impeded, thus decreasing the overall catalytic activity. It is also worth noting that the 10% F/BCN nanohybrid surpassed by far the electrocatalytic activity of the 5% F/BCN, showing an onset potential of −0.042 V vs RHE and a η_{10} of 222 mV, which places it between the most efficient metal-free carbon-based low-dimensional HER catalysts reported to date (Table S5). We believe that the optimal interfacial interactions for the 10% F/BCN hybrid provide higher structural defects that trigger an effective intramolecular ET and therefore more efficient active sites for HER.[39]

To gain further insights into the activity of the F/BCN hybrids, we employed density functional theory (DFT) calculations (see details in the Supporting Information) to obtain the ΔG_{H^*} values at the different F/BCN interfaces, which is an excellent descriptor to measure how the catalyst surfaces can thermodynamically impact the HER electrocatalysis. For the HER, in principle, the free energy of hydrogen adsorption (ΔG_{H^*}) for an ideal catalyst should be zero.[24] As we can see from Figure 3C, the value of ΔG_{H^*}(0.03 eV) for 10% F/BCN is the closest to zero, in agreement with the best HER performance. As the amount of F increases, the binding strength of the H on the active sites becomes stronger, which promotes slower kinetics for the catalysts. The volcano catalytic trends (Figure 3D) also showed that the 10% F/BCN nanocatalyst is located at the maximum of the peak, reinforcing

https://dx.doi.org/10.1021/jacs.0c12386
J. Am. Chem. Soc. 2021, 143, 1203−1215

that this catalyst shows the most efficient catalytic rates. The electrochemical active surface area (ECSA) of the nanohybrids were further calculated by using the double-layer capacitance methodology to verify the HER performance (Figure 3E and Figure S1).[39] The cyclic voltametric measurements were performed at different scan rates (5, 10, 20, 30, 40, and 50 mV/s) and potentials ranging from 0.1 to 0.3 V vs RHE. The differences between the anodic and cathodic currents at the non-faradaic region of the CV curves were plotted against the scan rates (mV/s) to obtain the C_{dl} (mF cm^{-2}) values. The C_{dl} for 10% F/BCN (5.55 mF cm^{-2}) was the largest value among all the catalysts as well as the ECSA (138.75 cm^2) and the RF (1982) (Table S1). The higher ECSA of 10% F/BCN demonstrates the existence of more available active sites on its surface, which is also responsible for the pronounced HER activity.[23] The current densities were also normalized by the measured ECSAs to investigate the intrinsic catalytic activity, and it was clear that the 10% F/BCN displayed the best performance in terms of onset potential and η_{10} (Figure 3F). The LSVs were then normalized by the TOF, and the 10% F/BCN nanohybrid still exhibited the best performance (Figure S6). Additionally, the higher turnover frequency (2.63), mass activity (137.97), and specific activity (0.14) values confirmed the best intrinsic catalytic properties of 10% F/BCN nanohybrid (Figure 3G and Table S2). As expected, the factors influencing the remarkable HER activity also played a crucial role toward the hydrogen oxidation reaction (HOR). Figure 3H compares the steady-state polarization curves of the F, BCN, and their nanohybrids in a H_2-saturated 0.5 M H_2SO_4 solution. Similar to HER, the electrocatalytic HOR performance follows the same order of 10% F/BCN > 5% F/BCN > 20% F/BCN > 30% F/BCN, being the 10% F/BCN best for HOR reaction as well. Particularly, the 10% F/BCN catalyst produced the largest current density value at 0.1 V (1.47 mA cm^{-2}). These findings are in good agreement with the theoretical ΔG_{H^*} value of −0.03 eV (as the HOR is the reverse of the HER), which reinforces that 10% F/BCN is the most active HOR catalyst.[40,41] Stability is also a key factor for evaluating the performance of electrocatalysts toward the HER and HOR processes for practical applications.[40,41] As seen in Figure 3I, the 10% F/BCN electrocatalyst displayed very good long-term stability for the HER reaction with the current density remaining almost unchanged after 12 h of operation and showed even better electrochemical stability performance that the benchmark Pt/C (Figure S7). The 10% F/BCN electrocatalyst also exhibited similar long-term stability performance during the HOR reaction (Figure 3I: inset). We have performed the UV−vis analysis of the 10% F/BCN nanohybrid sample before and after the stability test to verify if there any change in the $\pi-\pi$ interaction between the fullerene molecule and BCN network (Figure S8), and no significant changes were observed.

3.3. Oxygen Evolution and Reduction Reactions. The water oxidation electrocatalytic activity of the F/BCN hybrids was then evaluated in alkaline media (0.5 M NaOH) by using a standard three-electrode setup. The individual components (F and BCN) and a commercial RuO_2 catalyst were also studied and compared with the hybrids. Figure 4A displays the linear sweep voltammetry curves of the electrocatalysts at a scan rate of 2 mV s^{-1}. The dotted lines in Figure 4A indicate the overpotentials required to reach the current density of 10 mA cm^{-2}, which is used as a crucial figure of merit for OER catalytic materials.[24] Among all the studied materials, only 5% F/BCN, 10% F/BCN, and the RuO_2 benchmark catalyst achieved a η_{10} value. The 10% F/BCN dramatically surpassed the performances of all the materials tested. While the 10% F/BCN hybrid requires 390 mV to reach the current density of 10 mA cm^{-2}, the benchmark RuO_2 catalyst requires 410 mV. The remarkable catalytic activity and kinetics were further reflected by the Tafel slopes.[24] As shown in Figure 4B, the 10% F/BCN composite showed the lowest Tafel slope of 79 mV/dec, indicating the superior OER kinetics on the catalytic surfaces.[24] In summary, this new electrocatalyst is comparable with the state-of-the-art nonmetallic hybrid catalysts, and it is also comparable to the more kinetically active candidates for the OER process (Table S6).

The outstanding catalytic properties of 10% F/BCN can be understood on the basis of the unique electronic flow at the interfacial regions. As was described in the HER section, the interfacial interactions and defects are strongly connected with the intermolecular ET at the 0D−2D interfaces. For the 10% F/BCN hybrid, the distorted heteroatom motifs that are in contact with the fullerenes activate a very strong unidirectional electronic coupling from the lone pair electrons of the nitrogen atoms to the F cages, thus generating positive charges at the N atoms that can behave as highly efficient active sites for oxygen electrochemistry.[42] To demonstrate the effectiveness of 10% F/BCN hybrid in alkaline media (OER condition), we performed the electrochemical double-layer capacitance measurements (Figure 4C and Figure S2).[24] Figure 4C displays the Δj vs scan rate plot of the catalysts obtained at 1.2 V vs RHE. From these plots, the double-layer capacitance (C_{dl}) at the electrochemical interfaces as well as the ECSA and RF were calculated. Importantly, the 10% F/BCN catalyst delivered values of 4.61 mF cm^{-2}, 115 cm^2, and 1646 for C_{dl}, ECSA, and RF, respectively, which are much higher than those of the other F/BCN hybrids. These results demonstrate that the remarkable ET from the interfacial N atoms to the fullerenes induce the formation of the highest number of electrochemically active sites for OER. To unravel the intrinsic catalytic activity, the LSV plots of the catalysts were normalized by the corresponding ECSA values (Figure 4D). The 10% F/BCN catalyst still exhibits the lowest OER onset potential value (1.46 V vs RHE), indicating that its interfacial active sites initiate the water oxidation process more efficiently than the catalytic centers of the other hybrids. The improved SA and MA values of the 10% F/BCN are additional indicators that verify its superior intrinsic OER catalytic activity (Figure 4E and Table S3). The turnover frequency of 10% F/BCN at 1.7 V was estimated to be 1.14, which is 2 times better than the second-best electrocatalyst (5% F/BCN), revealing that the number of oxygen molecules produced by each catalytic center is optimal for the 10% F/BCN (Figure S3). The higher intrinsic catalytic performances of the 10% F/BCN nanomaterials was further confirmed by the TOF normalized current density vs potential plots (Figure 4F).

In-depth insights were obtained from the Gibbs free energy diagrams of the 0D−2D catalysts (Figure 4G). It is important to point out that the third step (*O → *OOH) is the rate-limiting step for the OER process for all the F/BCN composites.[24] We found that the local interactions as well as the pronounced intermolecular ET between the fullerenes and the BCN NSs for the 10% F/BCN system decrease the uphill energy states toward the formation of catalytic intermediates, thus facilitating water oxidation. In this regard, the O*, OH*, and OOH* intermediate catalytic species exhibited the most

https://dx.doi.org/10.1021/jacs.0c12386
J. Am. Chem. Soc. 2021, 143, 1203−1215

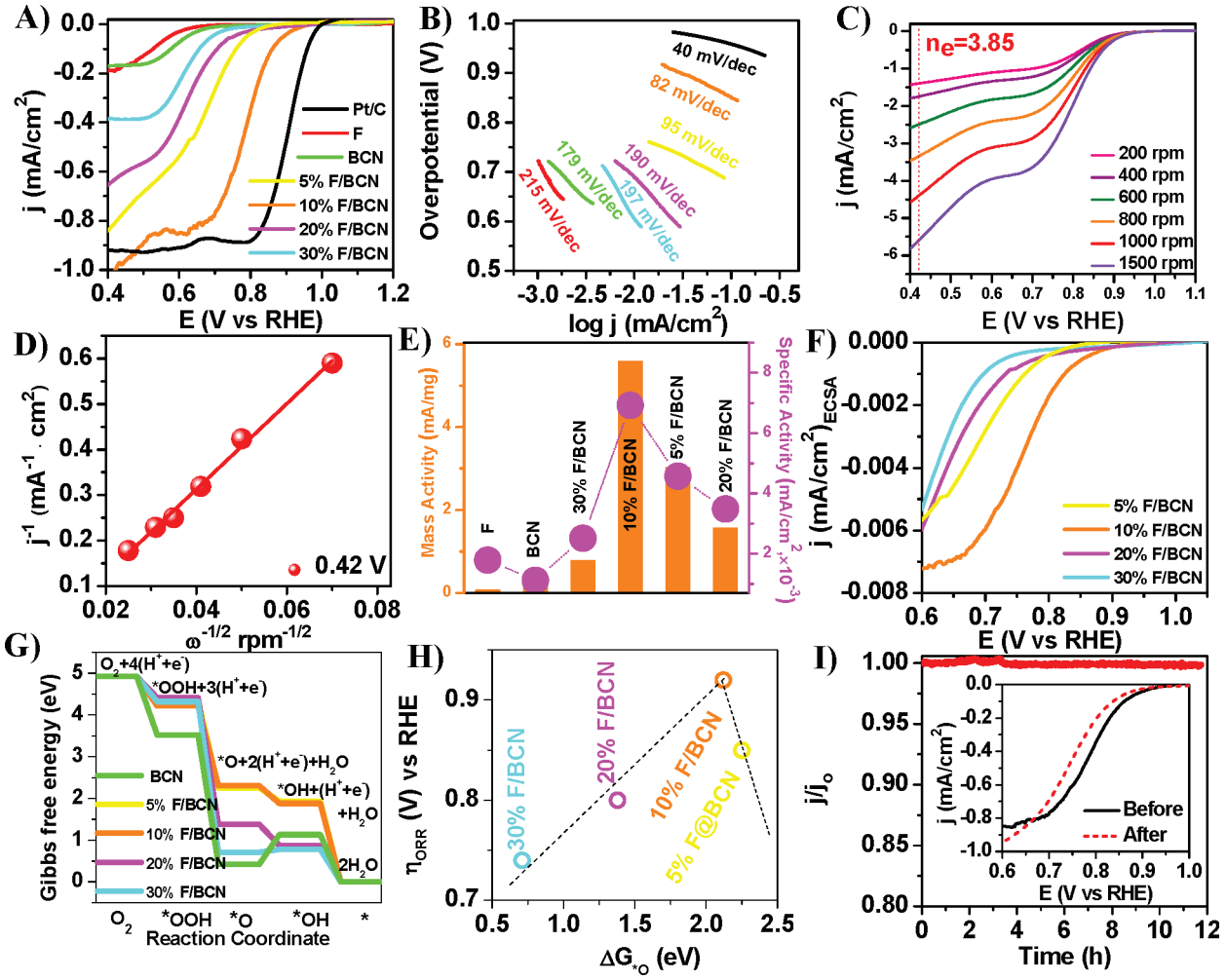

Figure 5. (A) LSV curves of F, BCN, 5% F/BCN, 10% F/BCN, 20% F/BCN, 30% F/BCN, and Pt/C for ORR at 2 mV s^{-1} in 0.5 NaOH. (B) The corresponding Tafel plots. (C) RDE voltammograms at various rotation rates from 200 to 1500 rpm at a scan rate of 10 mV/s. (D) K–L plots of the 10% F/BCN heterostructure. (E) MA and SA values for F, BCN, and their hybrids. (F) ECSA normalized LSV plots for the F/BCN nanohybrids. (G) Gibbs free energy diagram showing the differences of each elementary ORR catalytic step for both BCN and F/BCN nanohybrids. (H) Volcano plots of η_{ORR} vs ΔG_{*O}. (I) *I* vs *t* curve for 10% F/BCN at 0.75 V vs RHE, and the inset shows the comparison between the LSVs at the initial and after 1000 CV cycles.

energetically favorable ΔG values, which are 2.3, 1.8, and 4.22 eV, respectively, as well as a desirable rate-limiting potential of 0.69 eV, which is the lowest value among all the catalysts.[24] This is attributed to the moderate interaction between the reaction intermediates and the 10% F/BCN, leading to the best catalytic activity for the OER process. It is also worth pointing out that the 10% F/BCN nanohybrid is located at the top of the volcano curves, confirming the previous findings (Figure 4H). The durability of the 10% F/BCN catalyst was investigated for the OER process by performing 1000 CV cycles at 50 mV/s. A LSV measurement was performed right after the CV measurements and compared with the initial LSV measurement to examine the durability (Figure 4I: inset). It was observed that the current density change between the two LSVs was insignificant, demonstrating the excellent durable nature of the catalyst. Chronoamperometric measurements were further conducted to confirm the stability of 10% F/BCN for 12 h. Interestingly, the 10% F/BCN catalyst retained ~99.5% of the current density even after 12 h of operation, revealing its remarkable long-term stability features (Figure 4I). Also, it surpasses the stability of the benchmark OER RuO_2 electrocatalyst (Figure S9).

The electrochemical properties of the F/BCN catalysts toward the ORR reaction were also studied. Initially, cyclic voltametric (CV) measurements were conducted in a conventional three-electrode electrochemical cell in an O_2- or N_2-saturated 0.5 M NaOH solution at 50 mV s^{-1}. Figure S10 depicts a well-defined characteristic oxygen reduction peak for the 10% F/BCN hybrid at ~0.70 V vs RHE in an O_2-saturated NaOH solution. This peak is also observed for the other F/BCN catalysts, but at lower potential values, indicating their lower catalytic activities for the electroreduction of oxygen.[24,43] The ORR LSV polarization curves (Figure 5A) show that the 10% F/BCN exhibits an excellent ORR performance with an onset potential of 0.92 V, a half-wave potential of 0.79 V vs RHE, and a Tafel slope of 87 mV dec^{-1} (Figure 5B), which surpass the values exhibited by the other 0D–2D catalysts and are comparable to those of the state-of-the-art metal-free carbon-based electrocatalysts reported to date (Table S7). The ORR kinetics of the 10% F/BCN catalyst was further explored by using linear sweep voltammetry at different rotational speeds from 200 to 1500 rpm (Figure 5C). The corresponding Koutecky–Levich (K–L) plots revealed important insights into the kinetics of the interfacial redox reactions at the

https://dx.doi.org/10.1021/jacs.0c12386
J. Am. Chem. Soc. 2021, 143, 1203–1215

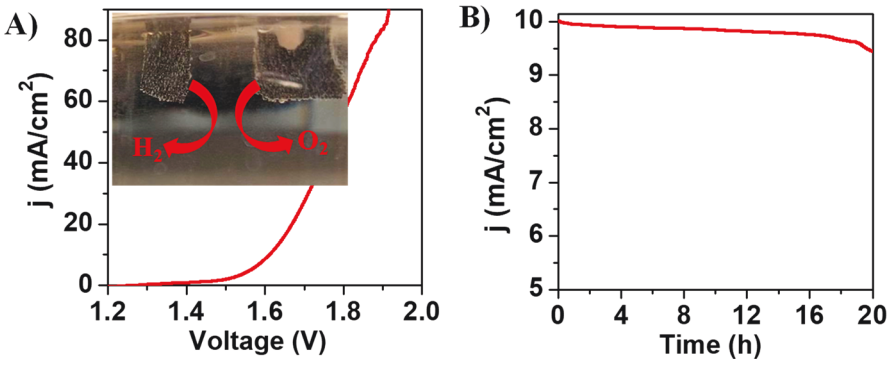

Figure 6. (A) LSV curve of the overall water splitting process using 10% F/BCN as both cathode and anode in a 0.5 M NaOH solution. The inset in (A) shows the digital photograph for producing O_2 (anode) and H_2 (cathode) bubbles on the 10% F/BCN modified carbon cloth electrodes. (B) Chronoamperometric measurements of 10% F/BCN for H_2O electrolysis at 1.61 V for 20 h.

catalytic surfaces of 10% F/BCN.[44,45] The linearity of the K−L plots of 10% F/BCN (Figure 5D) clearly establishes a first-order reaction kinetic process.[46,47] Furthermore, they show a very efficient four-electron reduction pathway since the calculated electron transfer number is 3.85 per O_2 molecule.[48]

The remarkable ORR electrocatalytic properties of 10% F/BCN are associated with the positively charged N active sites at the 0D−2D interfaces, which were previously explained. Additionally, the large number of pyridinic nitrogen atoms in the BCN nanosheet network of 10% F/BCN nanohybrid facilitates the oxygen adsorption by providing more Lewis base sites and reducing the energy barriers.[19] We also cannot rule out the influence of the B−C−N edge groups on the improved catalytic activity.[49] To investigate the intrinsic catalytic activity of the electrocatalysts, we have calculated the MA, SA, and TOF; and the results are presented in Figure 5E and Table S4. The 10% F/BCN hybrid exhibit the highest values. Furthermore, 10% F/BCN displays the best onset potential as well as a higher current density than the other hybrids after normalizing the ORR LSV polarization curves by their respective ECSAs (Figure 5F), indicating that this hybrid exhibits the greatest catalytic performance per active unit toward the ORR process. The Gibbs free energy values for all the hybrids were calculated to obtain mechanistic insights into the ORR electrocatalytic performance of the 0D−2D hybrids (Figure 5G). It is important to note that the third step (*O → *OH) is the rate-limiting step for the ORR process for all the F/BCN catalysts.[50,51] Noticeably, the 10% F/BCN shows the lowest rate-limiting potential (0.81 eV), thus decreasing the energy barrier for the rate-determining catalytic step, which, in turn, increases the reaction rates. Also, the 10% F/BCN heterostructure reached the top of the volcano plot, indicating its superior catalytic performance (Figure 5H). Considering the possibility of practical applications, we tested the durability of 10% F/BCN for the ORR reaction using the same methodology mentioned above in the OER section (Figure 5I: inset). The LSVs that were measured at the initial time and after CV measurements were plotted together and compared. There were very small changes in the onset potential and current density, indicating excellent durability. Additionally, the 10% F/BCN nanohybrid also demonstrated remarkable stability for the ORR process with respect to the benchmark Pt/C as seen in Figure 5I and Figure S11, making it an excellent candidate for practical applications.

3.4. Overall Water Splitting Application. Taking into consideration the remarkable HER and OER performances of the 10% F/BCN, a two-electrode configuration water electrolyzer was set up to study the overall water splitting reaction in a NaOH electrolyte (0.5 M), where the 10% F/BCN catalyst was loaded on carbon cloth to perform as both the anode and cathode. As Figure 6A depicts, the 10% F/BCN||10% F/BCN requires only a cell potential of 1.61 V to reach a current density of 10 mA cm^{-2}. Remarkably, the electrocatalytic performance of the 10% F/BCN||10% F/BCN electrolyzer is comparable and competitive with recently reported water splitting devices.[52−56] The inset in Figure 6A shows the digital image of the carbon cloth electrodes of the water splitting device. Many bubbles appear on the carbon cloths, demonstrating the effectiveness of the assembled overall water splitting system. Finally, the electrochemical stability of the 10% F/BCN catalyst was also investigated by conducting chronoamperometric measurements at 1.61 V (Figure 6B), and the current densities remain fairly stable (only 9% of the initial current lost) during the measurement period (i.e., 20 h), indicative of very good stability.

4. CONCLUSIONS

In summary, we report a new family of supramolecular F/BCN nanohybrid materials that exhibit tetrafunctional high-performance electrocatalysis for HER, HOR, OER, and ORR as well the ability to serve as a dual-purpose electrode for a single-cell device for water electrolysis. Using a combination of theory and experiment, we demonstrated that the metal-free 10% F/BCN nanohybrid material comprises a synergistic arrangement of the components that form a supramolecular interface with catalytic properties that exceed the electrochemical stability performance of existing commercial metal-based catalysts. The low manufacturing costs and the facile scalable synthesis of the new supramolecular material will pave the way to a new metal-free electrocatalysts for hydrogen and oxygen electrochemistry and related reactions that may have applications in emerging water treatment and energy storage technologies.

■ ASSOCIATED CONTENT

Supporting Information

The Supporting Information is available free of charge at https://pubs.acs.org/doi/10.1021/jacs.0c12386.

Computational methods; ECSA calculation; TOF calculation, comparison of HER, OER, and ORR performances of the as-synthesized electrocatalysts; the obtained C_{dl}, ECSA and RF values for different electrocatalysts in HER and OER conditions; compar-

https://dx.doi.org/10.1021/jacs.0c12386
J. Am. Chem. Soc. 2021, 143, 1203−1215

ison of HER, OER, and ORR performances of 10% F/BCN with previously reported metal-free electrocatalysts; XPS survey spectra of 10% F/BCN; UV−vis spectra of F and 10% F/BCN; UV−vis spectra of 10% F/BCN before and after HER stability test; TOF normalized LSVs for HER reaction; long-term stability of Pt/C for HER and ORR reactions and RuO_2 for OER reaction; CV measurements of the F/BCN electrocatalysts in N_2- and O_2-saturated solutions (PDF)

AUTHOR INFORMATION

Corresponding Authors

Juan C. Noveron − *Department of Chemistry and Biochemistry, University of Texas at El Paso, El Paso, Texas 79968, United States; Nanosystems Engineering Research Center for Nanotechnology-Enabled Water Treatment, Houston, Texas 77005, United States;* orcid.org/0000-0002-2762-7802; Email: jcnoveron@utep.edu

Alain R. Puente Santiago − *Department of Chemistry and Biochemistry, University of Texas at El Paso, El Paso, Texas 79968, United States*; Email: arpuentesan@utep.edu

Luis Echegoyen − *Department of Chemistry and Biochemistry, University of Texas at El Paso, El Paso, Texas 79968, United States;* orcid.org/0000-0003-1107-9423; Email: ezchegoyen@utep.edu

Authors

Md Ariful Ahsan − *Department of Chemistry and Biochemistry, University of Texas at El Paso, El Paso, Texas 79968, United States; Nanosystems Engineering Research Center for Nanotechnology-Enabled Water Treatment, Houston, Texas 77005, United States;* orcid.org/0000-0002-2024-8690

Tianwei He − *Centre for Materials Science and School of Chemistry and Physics, Science and Engineering Faculty, Queensland University of Technology, Brisbane, QLD 4000, Australia*

Kamel Eid − *Gas Processing Center, College of Engineering,, Qatar University, Doha 2713, Qatar;* orcid.org/0000-0001-5327-2497

Aboubakr M. Abdullah − *Center for Advanced Materials, Qatar University, Doha 2713, Qatar*

Michael L. Curry − *Department of Chemistry, Tuskegee University, Tuskegee, Alabama 36088, United States;* orcid.org/0000-0001-7026-9724

Aijun Du − *Centre for Materials Science and School of Chemistry and Physics, Science and Engineering Faculty, Queensland University of Technology, Brisbane, QLD 4000, Australia;* orcid.org/0000-0002-3369-3283

Complete contact information is available at: https://pubs.acs.org/10.1021/jacs.0c12386

Notes

The authors declare no competing financial interest.

ACKNOWLEDGMENTS

This research was funded in part by the US National Science Foundation (NSF) Nanotechnology-Enabled Water Treatment Center (NEWT ERC435 1449500) (to J.C.N.), the USDA 2019-38422-30214 (to J.C.N.), and the NSF CHE-18001317 (to L.E.). The Robert A. Welch Foundation is gratefully acknowledged for an endowed chair to L.E. (Grant AH-0033), and the Ralph & Kathleen Ponce de Leon Professorship to J.C.N is gratefully acknowledged. This work was also supported by the NPRP Grant NPRP10-0125-170252 from the Qatar National Research Fund (a member of the Qatar Foundation).

REFERENCES

(1) Puente Santiago, A. R.; Fernandez-Delgado, O.; Gomez, A.; Ahsan, M. A.; Echegoyen, L. Fullerenes as key components for low-dimensional (photo) electrocatalytic nanohybrid materials. *Angew. Chem., Int. Ed.* **2021**, *60*, 122−141.

(2) Chen, M.; Guan, R.; Yang, S. Hybrids of fullerenes and 2d nanomaterials. *Adv. Sci.* **2019**, *6* (1), 1800941.

(3) Voiry, D.; Shin, H. S.; Loh, K. P.; Chhowalla, M. Low-dimensional catalysts for hydrogen evolution and CO_2 reduction. *Nat. Rev. Chem.* **2018**, *2* (1), 0105.

(4) Gao, R.; Dai, Q.; Du, F.; Yan, D.; Dai, L. C_{60}-adsorbed single-walled carbon nanotubes as metal-free, pH-universal, and multifunctional catalysts for oxygen reduction, oxygen evolution, and hydrogen evolution. *J. Am. Chem. Soc.* **2019**, *141* (29), 11658−11666.

(5) Santiago, A. R. P.; He, T.; Eraso, O.; Ahsan, M. A.; Nair, A. N.; Chava, V. S.; Zheng, T.; Pilla, S.; Fernandez-Delgado, O.; Du, A. Tailoring the Interfacial Interactions of van der Waals 1T-MoS_2/C_{60} Heterostructures for High-Performance Hydrogen Evolution Reaction Electrocatalysis. *J. Am. Chem. Soc.* **2020**, *142* (42), 17923−17927.

(6) Zhang, L.; Lin, C. Y.; Zhang, D.; Gong, L.; Zhu, Y.; Zhao, Z.; Xu, Q.; Li, H.; Xia, Z. Guiding Principles for Designing Highly Efficient Metal-Free Carbon Catalysts. *Adv. Mater.* **2019**, *31* (13), 1805252.

(7) Jin, H.; Huang, H.; He, Y.; Feng, X.; Wang, S.; Dai, L.; Wang, J. Graphene quantum dots supported by graphene nanoribbons with ultrahigh electrocatalytic performance for oxygen reduction. *J. Am. Chem. Soc.* **2015**, *137* (24), 7588−7591.

(8) Li, Y.; Zhou, W.; Wang, H.; Xie, L.; Liang, Y.; Wei, F.; Idrobo, J.-C.; Pennycook, S. J.; Dai, H. An oxygen reduction electrocatalyst based on carbon nanotube−graphene complexes. *Nat. Nanotechnol.* **2012**, *7*, 394.

(9) Zhou, M.; Wang, S.; Yang, P.; Huang, C.; Wang, X. Boron carbon nitride semiconductors decorated with CdS nanoparticles for photocatalytic reduction of CO_2. *ACS Catal.* **2018**, *8* (6), 4928−4936.

(10) Zhang, M.; Zhou, M.; Luo, Z.; Zhang, J.; Wang, S.; Wang, X. Molten salt assisted assembly growth of atomically thin boron carbon nitride nanosheets for photocatalytic H_2 evolution. *Chem. Commun.* **2020**, *56* (17), 2558−2561.

(11) Lei, W.; Qin, S.; Liu, D.; Portehault, D.; Liu, Z.; Chen, Y. Large scale boron carbon nitride nanosheets with enhanced lithium storage capabilities. *Chem. Commun.* **2013**, *49* (4), 352−354.

(12) Zhou, M.; Chen, Z.; Yang, P.; Wang, S.; Huang, C.; Wang, X. Hydrogen reduction treatment of boron carbon nitrides for photocatalytic selective oxidation of alcohols. *Appl. Catal., B* **2020**, *276*, 118916.

(13) Hao, Y.; Wang, S.; Shao, Y.; Wu, Y.; Miao, S. High-Energy Density Li-Ion Capacitor with Layered SnS2/Reduced Graphene Oxide Anode and BCN Nanosheet Cathode. *Adv. Energy Mater.* **2020**, *10* (6), 1902836.

(14) Wang, S.; Ma, F.; Jiang, H.; Shao, Y.; Wu, Y.; Hao, X. Band gap-tunable porous Borocarbonitride nanosheets for high energy-density supercapacitors. *ACS Appl. Mater. Interfaces* **2018**, *10* (23), 19588−19597.

(15) Tabassum, H.; Zou, R.; Mahmood, A.; Liang, Z.; Guo, S. A catalyst-free synthesis of B, N co-doped graphene nanostructures with tunable dimensions as highly efficient metal free dual electrocatalysts. *J. Mater. Chem. A* **2016**, *4* (42), 16469−16475.

(16) Tabassum, H.; Guo, W.; Meng, W.; Mahmood, A.; Zhao, R.; Wang, Q.; Zou, R. Metal-organic frameworks derived cobalt phosphide architecture encapsulated into B/N Co-doped graphene nanotubes for all pH value electrochemical hydrogen evolution. *Adv. Energy Mater.* **2017**, *7* (9), 1601671.

(17) Zhang, H.; Ma, Z.; Duan, J.; Liu, H.; Liu, G.; Wang, T.; Chang, K.; Li, M.; Shi, L.; Meng, X.; Wu, K.; Ye, J. Active sites implanted carbon cages in core−shell architecture: highly active and durable electrocatalyst for hydrogen evolution reaction. *ACS Nano* **2016**, *10* (1), 684−694.
(18) Anjum, M. A. R.; Lee, M. H.; Lee, J. S. BCN network-encapsulated multiple phases of molybdenum carbide for efficient hydrogen evolution reactions in acidic and alkaline media. *J. Mater. Chem. A* **2017**, *5* (25), 13122−13129.
(19) Wang, J.; Hao, J.; Liu, D.; Qin, S.; Portehault, D.; Li, Y.; Chen, Y.; Lei, W. Porous boron carbon nitride nanosheets as efficient metal-free catalysts for the oxygen reduction reaction in both alkaline and acidic solutions. *ACS Energy Lett.* **2017**, *2* (2), 306−312.
(20) Barzegar, H. R.; Gracia-Espino, E.; Yan, A.; Ojeda-Aristizabal, C.; Dunn, G.; Wågberg, T.; Zettl, A. C_{60}/collapsed carbon nanotube hybrids: a variant of peapods. *Nano Lett.* **2015**, *15* (2), 829−834.
(21) Thirumalraj, B.; Palanisamy, S.; Chen, S.-M.; Lou, B.-S. Preparation of highly stable fullerene C_{60} decorated graphene oxide nanocomposite and its sensitive electrochemical detection of dopamine in rat brain and pharmaceutical samples. *J. Colloid Interface Sci.* **2016**, *462*, 375−381.
(22) Sariciftci, N. S.; Smilowitz, L.; Heeger, A. J.; Wudl, F. Photoinduced electron transfer from a conducting polymer to buckminsterfullerene. *Science* **1992**, *258* (5087), 1474−1476.
(23) Masa, J.; Weide, P.; Peeters, D.; Sinev, I.; Xia, W.; Sun, Z.; Somsen, C.; Muhler, M.; Schuhmann, W. Amorphous cobalt boride (Co_2B) as a highly efficient nonprecious catalyst for electrochemical water splitting: oxygen and hydrogen evolution. *Adv. Energy Mater.* **2016**, *6* (6), 1502313.
(24) Ahsan, M. A.; Puente Santiago, A. R.; Hong, Y.; Zhang, N.; Cano, M.; Rodriguez-Castellon, E.; Echegoyen, L.; Sreenivasan, S. T.; Noveron, J. C. Tuning of Trifunctional NiCu Bimetallic Nanoparticles Confined in a Porous Carbon Network with Surface Composition and Local Structural Distortions for the Electrocatalytic Oxygen Reduction, Oxygen and Hydrogen Evolution Reactions. *J. Am. Chem. Soc.* **2020**, *142* (34), 14688−14701.
(25) Ahsan, M. A.; Imam, M. A.; Santiago, A. R. P.; Rodriguez, A.; Alvarado-Tenorio, B.; Bernal, R.; Luque, R.; Noveron, J. C. Spent tea leaves templated synthesis of highly active and durable cobalt-based trifunctional versatile electrocatalysts for hydrogen and oxygen evolution and oxygen reduction reactions. *Green Chem.* **2020**, *22* (20), 6967−6980.
(26) Lei, W.; Portehault, D.; Dimova, R.; Antonietti, M. Boron carbon nitride nanostructures from salt melts: tunable water-soluble phosphors. *J. Am. Chem. Soc.* **2011**, *133* (18), 7121−7127.
(27) Vimalanathan, K.; Shrestha, R. G.; Zhang, Z.; Zou, J.; Nakayama, T.; Raston, C. L. Surfactant-free Fabrication of Fullerene C_{60} Nanotubules Under Shear. *Angew. Chem.* **2017**, *129* (29), 8518−8521.
(28) Huo, J.; Zeng, H. A novel triphenylamine functionalized bithiazole−metal complex with C_{60} for photocatalytic hydrogen production under visible light irradiation. *J. Mater. Chem. A* **2015**, *3* (12), 6258−6264.
(29) Yu, D.; Park, K.; Durstock, M.; Dai, L. Fullerene-grafted graphene for efficient bulk heterojunction polymer photovoltaic devices. *J. Phys. Chem. Lett.* **2011**, *2* (10), 1113−1118.
(30) Wang, S.; Iyyamperumal, E.; Roy, A.; Xue, Y.; Yu, D.; Dai, L. Vertically aligned BCN nanotubes as efficient metal-free electrocatalysts for the oxygen reduction reaction: a synergetic effect by co-doping with boron and nitrogen. *Angew. Chem., Int. Ed.* **2011**, *50* (49), 11756−11760.
(31) Ling, Z.; Wang, Z.; Zhang, M.; Yu, C.; Wang, G.; Dong, Y.; Liu, S.; Wang, Y.; Qiu, J. Sustainable synthesis and assembly of biomass-derived B/N co-doped carbon nanosheets with ultrahigh aspect ratio for high-performance supercapacitors. *Adv. Funct. Mater.* **2016**, *26* (1), 111−119.
(32) Wang, S.; Zhang, L.; Xia, Z.; Roy, A.; Chang, D. W.; Baek, J. B.; Dai, L. BCN graphene as efficient metal-free electrocatalyst for the oxygen reduction reaction. *Angew. Chem., Int. Ed.* **2012**, *51* (17), 4209−4212.
(33) Lai, L.; Potts, J. R.; Zhan, D.; Wang, L.; Poh, C. K.; Tang, C.; Gong, H.; Shen, Z.; Lin, J.; Ruoff, R. S. Exploration of the active center structure of nitrogen-doped graphene-based catalysts for oxygen reduction reaction. *Energy Environ. Sci.* **2012**, *5* (7), 7936−7942.
(34) Domínguez-Chávez, J. G.; Cortez-Maya, S.; Moggio, I.; Arias-Marín, E.; Klimova, T.; Lijanova, I.; Martínez-García, M. Double Molecular Antenna Pyrene−Bridge-Fullerene C_{60}. *Open Org. Chem. J.* **2010**, *4* (1), 15−23.
(35) Chubarova, E.; Melenevskaya, E. Y. Analysis of Interactions in Fullerene-solvent-polymer System by UV-spectroscopy. *Fullerenes, Nanotubes, Carbon Nanostruct.* **2008**, *16* (5−6), 640−643.
(36) Alargova, R. G.; Deguchi, S.; Tsujii, K. Stable colloidal dispersions of fullerenes in polar organic solvents. *J. Am. Chem. Soc.* **2001**, *123* (43), 10460−10467.
(37) Ji, H.-X.; Hu, J.-S.; Tang, Q.-X.; Song, W.-G.; Wang, C.-R.; Hu, W.-P.; Wan, L.-J.; Lee, S.-T. Controllable preparation of submicrometer single-crystal C_{60} rods and tubes trough concentration depletion at the surfaces of seeds. *J. Phys. Chem. C* **2007**, *111* (28), 10498−10502.
(38) Zhao, Y.; Yang, L.; Chen, S.; Wang, X.; Ma, Y.; Wu, Q.; Jiang, Y.; Qian, W.; Hu, Z. Can boron and nitrogen co-doping improve oxygen reduction reaction activity of carbon nanotubes? *J. Am. Chem. Soc.* **2013**, *135* (4), 1201−1204.
(39) Kibsgaard, J.; Tsai, C.; Chan, K.; Benck, J. D.; Nørskov, J. K.; Abild-Pedersen, F.; Jaramillo, T. F. Designing an improved transition metal phosphide catalyst for hydrogen evolution using experimental and theoretical trends. *Energy Environ. Sci.* **2015**, *8* (10), 3022−3029.
(40) Song, F.; Li, W.; Yang, J.; Han, G.; Yan, T.; Liu, X.; Rao, Y.; Liao, P.; Cao, Z.; Sun, Y. Interfacial sites between cobalt nitride and cobalt act as bifunctional catalysts for hydrogen electrochemistry. *ACS Energy Lett.* **2019**, *4* (7), 1594−1601.
(41) Sun, K.; Zhang, T.; Tan, L.; Zhou, D.; Qian, Y.; Gao, X.; Song, F.; Bian, H.; Lu, Z.; Dang, J.; et al. Interface Catalysts of Ni/Co_2N for Hydrogen Electrochemistry. *ACS Appl. Mater. Interfaces* **2020**, *12* (26), 29357−29364.
(42) Wang, S.; Yu, D.; Dai, L. Polyelectrolyte functionalized carbon nanotubes as efficient metal-free electrocatalysts for oxygen reduction. *J. Am. Chem. Soc.* **2011**, *133* (14), 5182−5185.
(43) Shao, M.; Chang, Q.; Dodelet, J.-P.; Chenitz, R. Recent advances in electrocatalysts for oxygen reduction reaction. *Chem. Rev.* **2016**, *116* (6), 3594−3657.
(44) Parvez, K.; Yang, S.; Hernandez, Y.; Winter, A.; Turchanin, A.; Feng, X.; Müllen, K. Nitrogen-doped graphene and its iron-based composite as efficient electrocatalysts for oxygen reduction reaction. *ACS Nano* **2012**, *6* (11), 9541−9550.
(45) Chen, S.; Bi, J.; Zhao, Y.; Yang, L.; Zhang, C.; Ma, Y.; Wu, Q.; Wang, X.; Hu, Z. Nitrogen-doped carbon nanocages as efficient metal-free electrocatalysts for oxygen reduction reaction. *Adv. Mater.* **2012**, *24* (41), 5593−5597.
(46) Zhang, P.; Sun, F.; Xiang, Z.; Shen, Z.; Yun, J.; Cao, D. ZIF-derived in situ nitrogen-doped porous carbons as efficient metal-free electrocatalysts for oxygen reduction reaction. *Energy Environ. Sci.* **2014**, *7* (1), 442−450.
(47) Yang, L.; Zeng, X.; Wang, W.; Cao, D. Recent progress in MOF-derived, heteroatom-doped porous carbons as highly efficient electrocatalysts for oxygen reduction reaction in fuel cells. *Adv. Funct. Mater.* **2018**, *28* (7), 1704537.
(48) Kumar, A.; Zhang, Y.; Liu, W.; Sun, X. The chemistry, recent advancements and activity descriptors for macrocycles based electrocatalysts in oxygen reduction reaction. *Coord. Chem. Rev.* **2020**, *402*, 213047.
(49) Wu, J.; Rodrigues, M. T. F.; Vajtai, R.; Ajayan, P. M. Tuning the Electrochemical Reactivity of Boron-and Nitrogen-Substituted Graphene. *Adv. Mater.* **2016**, *28* (29), 6239−6246.
(50) Tsai, H.-C.; Hsieh, Y.-C.; Yu, T. H.; Lee, Y.-J.; Wu, Y.-H.; Merinov, B. V.; Wu, P.-W.; Chen, S.-Y.; Adzic, R. R.; Goddard, W. A.,

https://dx.doi.org/10.1021/jacs.0c12386
J. Am. Chem. Soc. 2021, 143, 1203−1215

III DFT study of oxygen reduction reaction on Os/Pt core−shell catalysts validated by electrochemical experiment. *ACS Catal.* **2015**, *5* (3), 1568−1580.
(51) Lian, Y.; Yang, W.; Zhang, C.; Sun, H.; Deng, Z.; Xu, W.; Song, L.; Ouyang, Z.; Wang, Z.; Guo, J.; Peng, Y. Unpaired 3d Electrons on Atomically Dispersed Cobalt Centres in Coordination Polymers Regulate both Oxygen Reduction Reaction (ORR) Activity and Selectivity for Use in Zinc−Air Batteries. *Angew. Chem., Int. Ed.* **2020**, *59* (1), 286−294.
(52) Niu, H.-J.; Chen, Y.-P.; Sun, R.-M.; Wang, A.-J.; Mei, L.-P.; Zhang, L.; Feng, J.-J. Prussian blue analogue-derived CoFe nanocrystals wrapped in nitrogen-doped carbon nanocubes for overall water splitting and Zn-air battery. *J. Power Sources* **2020**, *480*, 229107.
(53) Qin, Q.; Jang, H.; Chen, L.; Nam, G.; Liu, X.; Cho, J. Low loading of RhxP and RuP on N, P codoped carbon as two trifunctional electrocatalysts for the oxygen and hydrogen electrode reactions. *Adv. Energy Mater.* **2018**, *8* (29), 1801478.
(54) Yin, J.; Li, Y.; Lv, F.; Lu, M.; Sun, K.; Wang, W.; Wang, L.; Cheng, F.; Li, Y.; Xi, P.; Guo, S. Oxygen vacancies dominated NiS_2/CoS_2 interface porous nanowires for portable Zn−air batteries driven water splitting devices. *Adv. Mater.* **2017**, *29* (47), 1704681.
(55) Gao, X.; Zhang, H.; Li, Q.; Yu, X.; Hong, Z.; Zhang, X.; Liang, C.; Lin, Z. Hierarchical $NiCo_2O_4$ hollow microcuboids as bifunctional electrocatalysts for overall water-splitting. *Angew. Chem., Int. Ed.* **2016**, *55* (21), 6290−6294.
(56) Babar, P.; Lokhande, A.; Shin, H. H.; Pawar, B.; Gang, M. G.; Pawar, S.; Kim, J. H. Cobalt iron hydroxide as a precious metal-free bifunctional electrocatalyst for efficient overall water splitting. *Small* **2018**, *14* (7), 1702568.

https://dx.doi.org/10.1021/jacs.0c12386
J. Am. Chem. Soc. 2021, 143, 1203−1215

JACS
JOURNAL OF THE AMERICAN CHEMICAL SOCIETY
pubs.acs.org/JACS
Addition/Correction

Correction to "Tuning the Intermolecular Electron Transfer of Low-Dimensional and Metal-Free BCN/C_{60} Electrocatalysts via Interfacial Defects for Efficient Hydrogen and Oxygen Electrochemistry"

Md Ariful Ahsan, Tianwei He, Kamel Eid, Aboubakr M. Abdullah, Michael L. Curry, Aijun Du, Alain R. Puente Santiago,* Luis Echegoyen,* and Juan C. Noveron*

J. Am. Chem. Soc. **2021**, *143* (2), 1203−1215. DOI: 10.1021/jacs.0c12386

The acknowledgement of an NSF grant by L.E. was incorrectly referenced as CHE-18001317; the correct grant number is CHE-1801317. The full corrected Acknowledgement is included in this Correction.

■ ACKNOWLEDGMENTS

This research was funded in part by the US National Science Foundation (NSF) Nanotechnology-Enabled Water Treatment Center (NEWT ERC435 1449500) (to J.C.N.), the USDA 2019-38422-30214 (to J.C.N.), and the NSF CHE-1801317 (to L.E.). The Robert A. Welch Foundation is gratefully acknowledged for an endowed chair to L.E. (Grant AH-0033), and the Ralph & Kathleen Ponce de Leon Professorship to J.C.N. is gratefully acknowledged. This work was also supported by the NPRP Grant NPRP10-0125-170252 from the Qatar National Research Fund (a member of the Qatar Foundation).